Solar RRL
www.solar-rrl.com

Proton Radiation Hardness of Organic Photovoltaics: An In-Depth Study

Harrison Ka Hin Lee, Katherine Stewart, Declan Hughes, Jérémy Barbé, Adam Pockett, Rachel C. Kilbride, Keith C. Heasman, Zhengfei Wei, Trystan M. Watson, Matthew J. Carnie, Ji-Seon Kim, and Wing Chung Tsoi**

Recent developments of solution-processed bulk-heterojunction organic photovoltaic (OPV) cells have demonstrated power conversion efficiencies (PCEs) as high as 18% for single-junction devices. Such a high PCE in addition to its desirable lightweight property and high mechanical flexibility can realize high specific power and small stowed volume, which are key considerations when choosing PV for space missions. To take one important step forward, their resilience to ionizing radiation should be well studied. Herein, the effect of proton irradiation at various fluences on the performance of benchmark OPV cells is explored under AM0 illumination. The remaining device performance is found to decrease with increasing proton fluence, which correlates to changes in electrical and chemical properties of the active layer. By redissolving the devices, the solubility of the active layer is found to decrease with increasing proton fluence, suggesting that the active materials are likely cross-linked. Additionally, Raman studies reveal conformational changes of the polymer leading to a higher degree of energetic disorder. Despite a drop in performance, the retaining percentage of the performance is indeed higher than the current market-dominating space PV technology—III–V semiconductor-based PV, demonstrating a high potential of the OPV cell as a candidate for space applications.

1. Introduction

Organic photovoltaic (OPV) cell is redrawing much attention from both academic and industrial communities due to the recent breakthrough of over 18% power conversion efficiency (PCE) for single-junction devices, thanks to the invention of a new generation of nonfullerene-based small molecule acceptors.[1,2] With the much improved performance, in addition to light weight and highly flexible features of OPV devices, it is expected to deliver high specific power (power generation per unit mass) and small stowed volume. Such characteristics are key criteria for PV applications in space. A few works have demonstrated high specific power of 10–14 W g^{-1} using OPV cells, exhibiting values 10–100 times higher than that of inorganic cells.[3–5] Additionally, OPV cells can be ultrathin and extremely flexible which allow the cell to wrap around a human hair.[3–5] These properties are of paramount importance to PV devices used in space, as they reduce the launch weight, volume, and consequently the cost.

In addition to device performance, device stability is another key area of concern when considering a new PV technology operating in space, which may not be directly relevant to the stability for usual outdoor or indoor environments. Oxygen, moisture, and their combination with light are the primary causes of terrestrial OPV degradation.[6–8] However, in space, a number of stress factors such as extreme temperature cycling, thermal shock, ultrahigh vacuum exposure,

H. K. H. Lee, D. Hughes, J. Barbé, A. Pockett, Z. Wei, T. M. Watson, M. J. Carnie, W. C. Tsoi
SPECIFIC
College of Engineering
Swansea University
Swansea SA1 8EN, UK
E-mail: K.H.Lee@Swansea.ac.uk; w.c.tsoi@swansea.ac.uk

The ORCID identification number(s) for the author(s) of this article can be found under https://doi.org/10.1002/solr.202101037.

DOI: 10.1002/solr.202101037

H. K. H. Lee
Department of Physics
City University of Hong Kong
Kowloon, Hong Kong SAR, China

K. Stewart, J.-S. Kim
Department of Physics and Centre for Plastic Electronics
Imperial College London
London SW7 2AZ, UK

R. C. Kilbride
Department of Physics and Astronomy
The University of Sheffield
Sheffield S3 7RH, UK

K. C. Heasman
Ion Beam Centre
Advanced Technology Institute
University of Surrey
Guildford, Surrey GU2 7XH, UK

and ionizing radiation are all potential causes of degradation which must be taken into consideration. Among them, ionizing radiation could be the most critical as it is powerful and thus result in unpredictable degradation. Such radiation refers to X-rays, gamma rays, protons, neutrons, electrons, and heavy ions which primarily originate from cosmic rays and solar particle events.

Researchers in the OPV field have conducted some initial studies on how ionizing radiation affects OPV materials and devices. There are a few studies that have observed morphological and device performance degradation as a result of X-ray exposure in polymer:fullerene systems such as P3HT:PCBM.[9–13] Despite signs of degradation, P3HT:PCBM is still stable enough upon X-rays exposure for applications in space. Martynov et al. explored the effect of gamma rays on two polymer:fullerene systems and found that PCDTBT:PCBM system maintained approximately 90% of initial efficiency after exposure to a high radiation dose of 6500 Gy.[14] Other studies focused on electron and proton irradiation. For example, Bebensee et al. found that electron irradiation with an energy of 100 eV on P3HT causes the formation of C=C between the side chain of P3HT while the aromatic thiophene was unaffected.[15] Lee et al. showed a drop in absorption of P3HT:PCBM film after proton irradiation of 200 MeV.[16] On the contrary, our previous study of proton and electron irradiations on four OPV blend films, namely, PCDTBT:$PC_{71}BM$, PBDB-T:$PC_{71}BM$, PBDB-T:ITIC, BTR:$PC_{71}BM$, showed that they are chemically stable and photostable against low fluence of 10^{12} p cm^{-2} and 10^{13} e cm^{-2} with particle energy of 150 keV and 1 MeV, respectively.[17] In addition to the space-condition mimicking studies done on Earth, there are studies looking at the extraterrestrial behavior of OPV cells. Cardinaletti et al. mounted OPV cells to a balloon and sent them out for a 3 h stratospheric flight and the cells were survived with only 10–20% drop in PCE for polymer:fullerene cells.[18] Recently, Reb et al. reported the launch of OPV cells on a suborbital rocket flight and demonstrated in situ power generation of OPV cells under real space condition.[19]

In this study, the effect of 150 keV proton irradiation with fluence from 10^{12} to 10^{15} p cm^{-2} on the performance of OPV cells was investigated. Air mass 0 (AM0) was used for performance evaluation to replicate the illumination in space. It is well known that darkening effect happens on glass after particle irradiation,[20] hence quartz substrates were used for device fabrication in this work. The devices were purposely not encapsulated for this fundamental study as epoxy and cover glass may induce potential routes of degradation although encapsulation is unavoidable for real-world applications, especially in space. After completing the device fabrication, the devices were characterized in-house, sent out for proton irradiation with a set of devices as control (travel together but without underwent proton irradiation), and finally sent back for evaluation of the PV performance and advanced characterizations, which probe the charge carrier dynamic, optical properties, surface topography, and structural properties in molecular level. The whole period of one set of experiment took up to a month which is a rather long period of time for unencapsulated OPV cells although they were packed in nitrogen when they were sent from one laboratory to another. As a result, it is crucial to choose a fairly stable OPV system and device architecture for this experiment, especially the stability in air, in order to isolate the degradation due to proton. In terms of device architecture, inverted architecture was employed as it can avoid using low work function metals as the top electrode which can be air sensitive. After screening a number of benchmark OPV systems including polymer:fullerence and polymer:nonfullerene systems, poly[4,8-bis(5-(2-ethylhexyl)thiophen-2-yl)benzo[1,2-b;4,5-b']dithiophene-2,6-diyl-alt-(4-(2-ethylhexyl)-3-fluorothieno[3,4-b]thiophene-)-2-carboxylate-2-6-diyl)]:[6,6]-phenyl-C71-butyric acid methyl ester (PTB7-Th:$PC_{71}BM$) was selected for this study as the control cells showed excellent stability throughout the experiments (see Figure S1, Supporting Information).

2. Results and Discussion

2.1. Simulations on Proton Bombardment

To understand the proton penetration behavior on the organic photoactive materials, simulations of proton irradiation on PTB7-Th:$PC_{71}BM$ with a series of proton energy were performed. Typically, in space, proton energy ranges from keV to MeV.[21] A higher proton energy represents a higher probability of penetration into a given material which leads to less energy loss within the materials and probably less degradation. To study the penetration of proton into the material, simulations of the proton energy loss per unit depth were performed. To enhance the degradation effect, a higher proton energy loss per unit depth is preferred which corresponds to lower proton energy. **Figure 1**a shows the simulation of the proton energy loss against the depth of PTB7-Th:$PC_{71}BM$ with a series of proton energy from 50 keV to 10 MeV. From the simulations, 150 keV proton energy was chosen because it offers both sufficient penetration depth and high proton energy loss.

To confirm the penetration depth of 150 keV protons, the distribution of the proton stopping positions throughout the device configuration of quartz/AZO/ZnO/PTB7-Th:$PC_{71}BM$/MoO_3/Ag was simulated. Figure 1b visualizes the trajectories and penetration of protons into a device. In this case, most protons are stopped in the aluminum zinc oxide (AZO) bottom electrode layer while a small amount of protons are stopped in the PTB7-Th:$PC_{71}BM$ (but still significantly more than using higher energy protons such as in the range of MeV), MoO_3, ZnO, and Ag layers. A small number of protons penetrate as far as the quartz substrate but almost no protons penetrate the complete device stack.

2.2. Impact of Proton Irradiation on the Performance of OPV Device

The changes in performance of PTB7-Th:$PC_{71}BM$ devices due to exposure to 150 keV proton with fluence ranged from 10^{12} to 10^{15} p cm^{-2} were studied. **Figure 2**a shows the evolution of current density–voltage (J–V) characteristics of PTB7-Th:$PC_{71}BM$ devices under AM0 illumination (with intensity of 136.6 mW cm^{-2}) after exposure to proton irradiation (see **Table 1** for the corresponding device parameters). Comparison of the J–V curves and the device parameters under AM0 and AM1.5G is available in Figure S2 and Table S1, Supporting Information. The influence of proton irradiation on the J–V

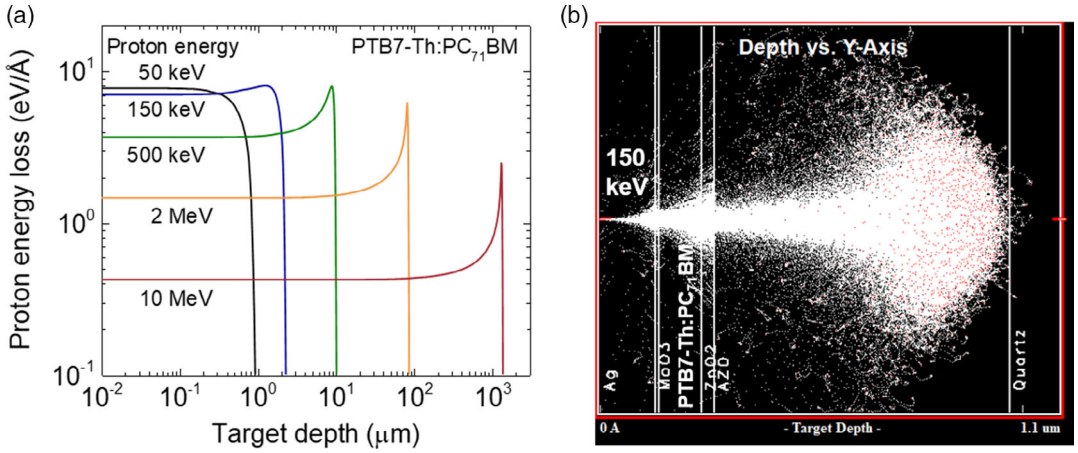

Figure 1. Simulations of proton irradiation on PTB7-Th:$PC_{71}BM$ films and devices. a) Proton energy loss as a function of depth in PTB7-Th:$PC_{71}BM$. b) Distribution of the stopping positions of 150 keV protons in a device with a configuration of quartz/AZO/ZnO/PTB7-Th:$PC_{71}BM$/MoO_3/Ag.

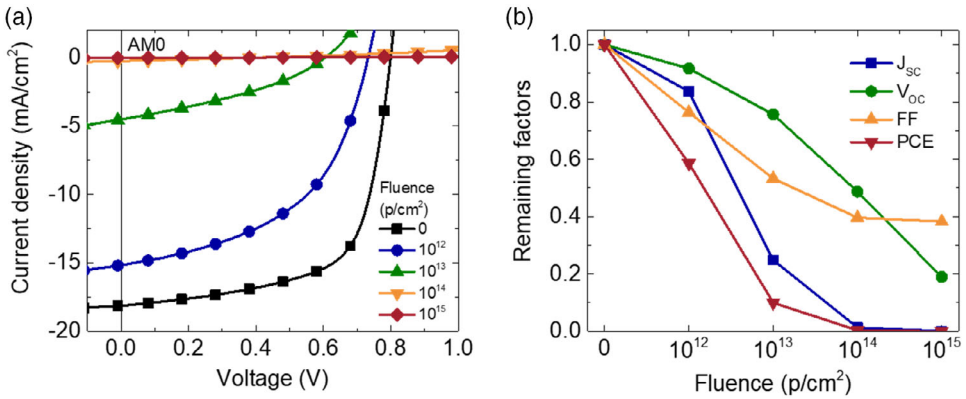

Figure 2. a) *J–V* characteristics of the OPV devices with and without proton irradiation under AM0 illumination. b) Remaining factors of the devices. (Plots without normalization are displayed in Figure S3, Supporting Information).

Table 1. Device parameters of the representative OPV devices under AM0 illumination with and without proton irradiation. Statistical data are available in Table S2, Supporting Information.

Fluence [p cm^{-2}]	J_{SC} [mA cm^{-2}]	V_{OC} [V]	FF [%]	PCE [%]
0	18.1	0.799	65.7	7.0
10^{12}	15.2	0.732	50.2	4.1
10^{13}	4.51	0.604	35.0	0.70
10^{14}	0.24	0.389	26.1	0.02
10^{15}	0.01	0.152	25.1	0.0003

curves can be clearly observed for all fluences applied herein. The remaining factors of the device parameters (compared to the control one) are calculated and plotted in Figure 2b. For the lowest fluence 10^{12} p cm^{-2}, the PCE drops to 58.6% of the control device due to ≈16%, 8%, and 24% drop in short-circuit current density (J_{sc}), open-circuit voltage (V_{oc}), and fill factor (FF), respectively. For 10^{13} p cm^{-2}, further decreases were observed for all parameters with a more pronounced drop in the J_{sc}, a further drop of 59%, resulting in a PCE of 0.7%. For higher fluences of 10^{14} and 10^{15} p cm^{-2}, the *J–V* curves were nearly flat in the region of interest when compared to the others, suggesting nearly 0% PCE of the control device, due to very limited photocurrent generation. It is worth noting that the control device was not just a fresh device. Instead, it travelled together with all other samples being irradiated and the *J–V* was scanned when all the samples came back. This allows isolation of the effect of the intrinsic degradation during the transport, although we found that the degradation is in fact very minimal in this OPV system (see Figure S1, Supporting Information).

2.3. Charge Recombination and Transport Studies

To gain more understanding on the degradation of the device parameter, here we studied the charge recombination and transport by a combination of transient photovoltage (TPV) and transient photocurrent (TPC) measurements, and photoinduced charge carrier extraction in a linearly increasing voltage (photo-CELIV), respectively.[22–24] These techniques can only probe functioning PV devices. For the devices that underwent

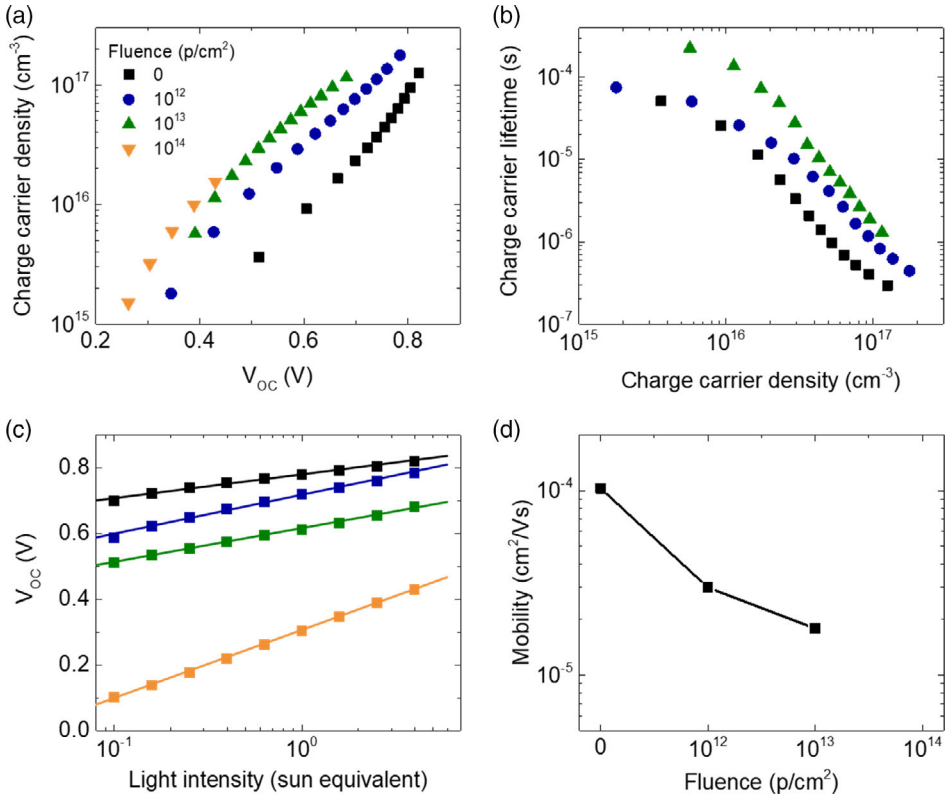

Figure 3. a) Charge density, n, as a function of V_{oc}, b) recombination lifetimes, τ, extracted from TPV measurements as a function of charge density, c) V_{oc} as a function of light intensity, and d) fastest carrier mobility extracted from photo-CELIV measurement for the OPV cells underwent different fluences.

fluences of 10^{14} and 10^{15} p cm^{-2}, their PV behavior is hardly observed so data obtained from these techniques may not be well resolved for analysis. **Figure 3**a shows the charge carrier density, n, plotted as a function of V_{oc} of the devices. Proton-irradiated devices show lower V_{oc} with increasing fluence exposure at a given charge carrier density. In other words, for higher fluence, there is a higher charge carrier density at a given V_{oc}, which could suggest increased trap formation upon higher fluence.[25–28] The formation of traps could arise from radiation-induced defects. The increase in charge carrier density upon proton irradiation with increasing fluence is consistent with the observed drops in the V_{oc} obtained in the J–V sweeps. Trap states could be formed during the proton irradiation which results in increased trap-assisted recombination, and thus lower V_{oc}.

Figure 3b shows the charge carrier lifetimes which are extracted by fitting a monoexponential function to the TPV decay. A good fit with a monoexponential function suggests that the degradation in device performance does not involve additional dominant recombination processes such as interfacial recombination (see Figure S4, Supporting Information, for representative voltage decays and corresponding fitting). Increased charge carrier lifetimes are obtained for increasing fluence at a given charge carrier density. If the trap levels within the active layer are shallow, charge carriers will have a longer lifetime at a given charge carrier density which is the consequence of successive trapping and detrapping events happened before they are finally extracted or recombined.[25,26] This result supports the hypothesis that trap states are formed upon proton irradiation.

Along with the TPV and TPC measurements, diode ideality factors of the devices are extracted from the V_{oc} against light intensity plot as shown in Figure 3c, which can indicate the dominating type of the recombination.[29] For the control device, as expected, the ideality factor is close to the ideal value 1.[29] For devices exposed to proton irradiation, ideality factors show an overall increasing trend with increasing proton fluence. A higher ideality factor suggests domination of trap-assisted recombination in the active layer.[29] The results here qualitatively agree with the findings in the TPC and TPV studies.

Photo-CELIV is one of the most recognized techniques to evaluate charge carrier mobility in a PV device configuration, which probes the faster carrier in the device.[30] Figure 3d shows that the mobilities calculated from the peak times obtained from the transients (see Figure S5, Supporting Information) drop by more than 5 times, from 1.03×10^{-4} cm^2 V^{-1}s^{-1} for the control to 1.79×10^{-5} cm^2 V^{-1}s^{-1} for the fluence of 10^{13} p cm^{-2}, which agrees with the previous results that increased recombination is found in the irradiated devices due to shallow trap state formation.[8]

2.4. Spectroscopic Studies

The spectral responses of the devices were studied by conducting external quantum efficiency (EQE) measurement. The EQE spectra of the devices at different proton fluences are shown in **Figure 4**a. For all spectra, they show a noticeable bumpy feature

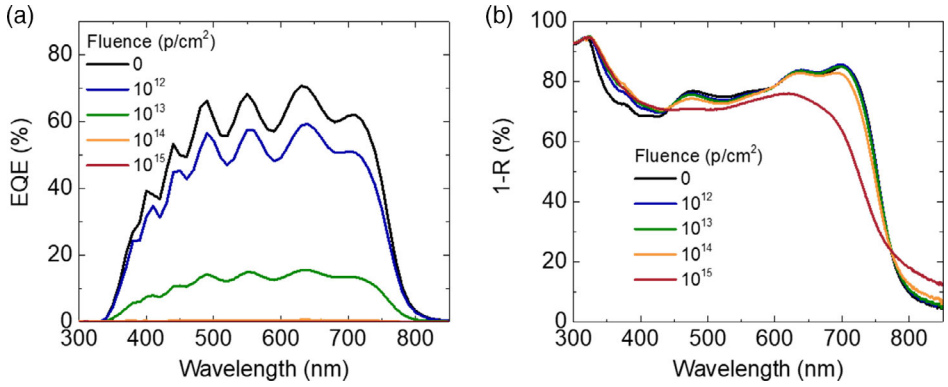

Figure 4. a) EQE spectra and b) absorption spectra of the control and irradiated samples obtained by reflectance measurement.

throughout the spectra which originates from the bottom transparent electrode, AZO (see Figure S6, Supporting Information, for the transmission of the AZO). For devices that underwent proton irradiation, the entire EQE spectra decrease with increasing proton fluence. This trend is consistence with the decrease in the J_{SC}, as shown in Figure 2a.

To understand the drops in the EQE (or J_{sc}) upon proton exposure, we checked the absorption spectra of the active materials via measuring 1–reflectance (R). The 1–R spectra (Figure 4b) of the samples (quartz/PTB7-Th:$PC_{71}BM$/MoO_3/Ag) only show little changes upon proton irradiation even up to fluence of 10^{14} p cm^{-2}. These little optical changes cannot account for the significant drops in the EQE spectra. The main origin of the losses in the photocurrent after proton irradiation is not due to the drop in absorption but due to other reasons such as more severe recombination. When the fluence reaches 10^{15} p cm^{-2}, the changes in the 1–R spectrum become more noticeable. The polymer peaks (≈639 nm and 698 nm) seem blueshifted and become less clear while one of the $PC_{71}BM$ peaks (479 nm) diminishes but the other $PC_{71}BM$ peak (323 nm) is still clearly displayed. These results suggest that PTB7-Th and $PC_{71}BM$ may have different degrees of degradation after the proton irradiation.

2.5. Surface Topography and Solubility Studies

Atomic force microscopy (AFM) was performed to study the impact of the surface topography upon proton irradiation. **Figure 5**a–e shows the height profile of the active layers on the devices where they are not covered by any interlayers and electrodes. Overall, they have a similar surface topography, with submicron scale granular features across all fluences. For the control sample and the proton irradiated samples with fluence up to 10^{14} p cm^{-2}, they show a moderate surface root mean square roughness of 3.4–3.6 nm. For 10^{15} p cm^{-2}, the surface is slightly smoother with a root mean square roughness of 2.4 nm, suggesting no significant change in the surface topography upon radiation.

To understand more about what has happened to the active layer, we redissolve the active layer by immersing the entire device into chlorobenzene on a hotplate of 120 °C. Figure 5f shows the appearance of the devices after redissolving. The control device becomes colorless, as expected, indicating good solubility of the PTB7-Th and $PC_{71}BM$. As the entire blend layer was dissolved, the top interlayer and the metal electrode (which sit on the active layer) were also removed and were visibly suspended in the solution. Interestingly, this scenario only happened to the control device and the device which underwent the lowest fluence 10^{12} p cm^{-2}. For those devices that underwent higher fluences (10^{13}–10^{15} p cm^{-2}), we observed that the color of the remaining active layer materials on the substrate was deeper with increasing fluence, suggesting that the PTB7-Th and/or $PC_{71}BM$ are less soluble and are retaining more on the devices. For the device exposed to 10^{15} p cm^{-2} proton fluence, the appearance is very similar in color to the one before redissolving. This observation is consistent with that the polymer PTB7-Th and/or $PC_{71}BM$ are partly cross-linked after 150 keV proton irradiation and the degree of cross-linking increases with the amount of fluence.[31] Cross-linking of OPV polymers was observed before under light stress.[32] This light-induced cross-linking is believed to form defects and traps for charge carriers, and severely affects the photovoltaic performance especially in the initial stage of the operation.

The absorbances of the solutions (see Figure 5g) obtained above were then examined. The absorbance drops gradually with increasing fluence as shown in Figure 5h, consistent with the visual observation as shown in the image (Figure 5f). The introduction of the insoluble materials is likely due to the cross-linking between the polymer chains and/or the fullerene-based small molecule. The spectra are normalized to a $PC_{71}BM$ absorption peak at 457 nm (Figure 5i). It is found that the relative peak ratios of the PTB7-Th peaks (≈626 nm and ≈698 nm) to the 457 nm $PC_{71}BM$ peak vary substantially with increasing fluence. At 10^{12} p cm^{-2}, the peak heights are all comparable, similar to the control. Basically, all the active layer materials are soluble, consistent with no cross-linking happened or only a low degree of cross-linking. At 10^{13} and 10^{14} p cm^{-2}, the intensity of the PTB7-Th peaks relative to the 457 nm peak drop to about half, meaning that a larger fraction of PTB7-Th becomes relatively less soluble when compared to the $PC_{71}BM$ counterpart and cross-linking could mainly happen in the PTB7-Th. At 10^{15} p cm^{-2}, the PTB7-Th peak heights are comparable again to the height at 457 nm although the 457 nm peak has in fact disappeared, suggesting that the dissolved $PC_{71}BM$ is very limited. From 10^{14} to 10^{15} p cm^{-2}, the solubility of $PC_{71}BM$ is relatively much reduced. At 10^{15} p cm^{-2}, the overall absorbance is very

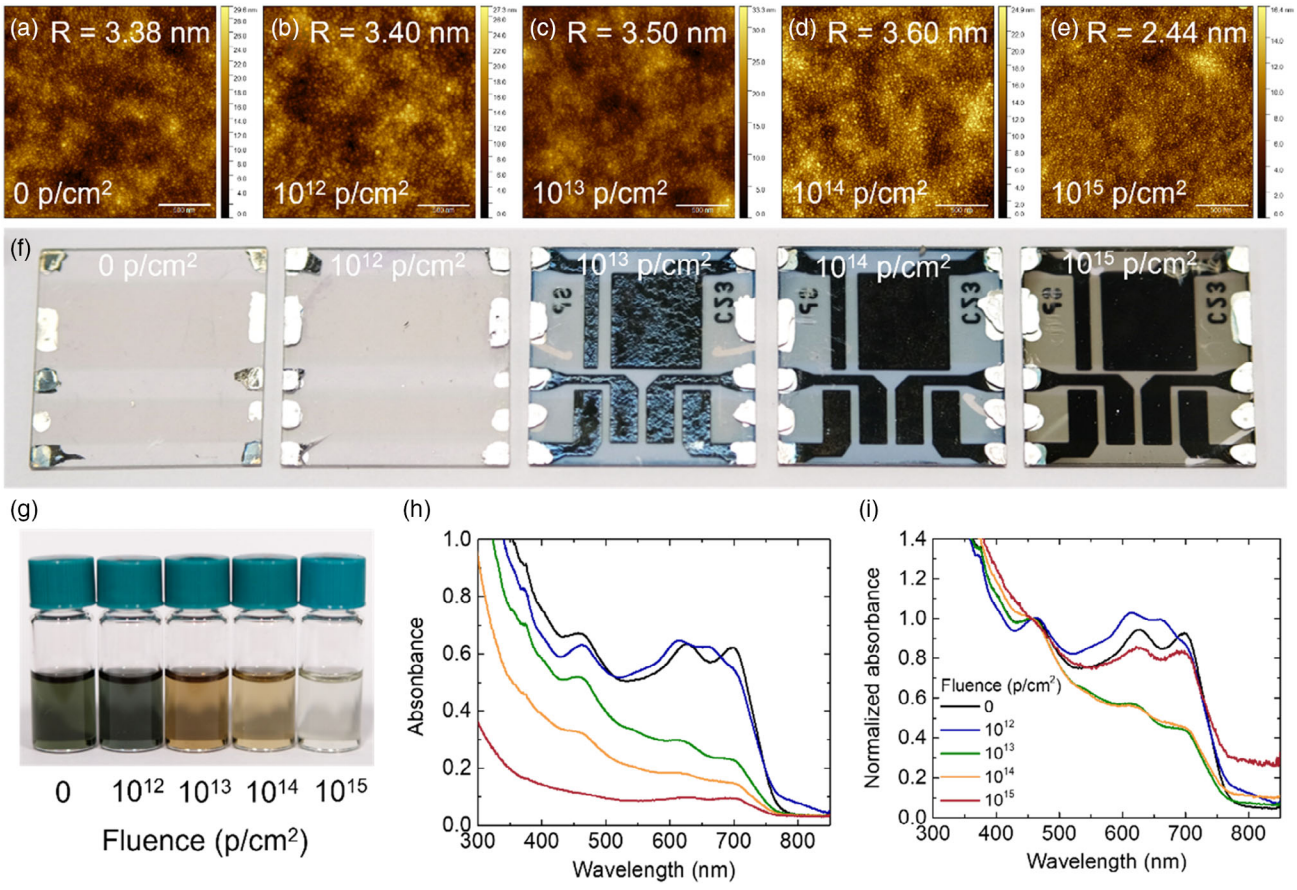

Figure 5. a–e) AFM height profiles of PTB7-Th:$PC_{71}BM$ on devices between the top electrodes. The scan area is 2 μm × 2 μm and the scale bars shown are 500 nm. f) Image of the proton irradiated devices after redissolving in chlorobenzene. g) Filtered solution collected from redissolving the devices in chlorobenzene. h) Absorbance of the solution obtained from redissolving the PTB7-Th:$PC_{71}BM$ devices. i) Normalized absorbance of (h) to the $PC_{71}BM$ peak at 457 nm.

low, about 0.1 within the visible region, meaning that the solubility of both materials is comparably low and tends to be consistent with the degree of cross-linking of the two materials being similar.

2.6. Conformational Change of the Polymer Probed by Raman Spectroscopy

To understand possible molecular origins inducing changes in molecular conformation and structure upon proton irradiation, Raman spectroscopy is used. The Raman spectra of the PTB7-Th:$PC_{71}BM$ blend were assigned by density functional theory (DFT) simulation of the polymer and fullerene components, as shown in Figure S7a, Supporting Information. The prominent peaks in the region of 1400–1550 cm^{-1} are attributed to the PTB7-Th backbone; the spectral assignment is shown on the polymer structure in Figure S7b, Supporting Information, and described in Figure S7c, Supporting Information.

The active layers of the proton irradiated devices within the active area were studied by Raman spectroscopy. First, we consider spectral changes across the whole Raman spectra. **Figure 6**a shows the Raman spectra of the proton-irradiated devices in comparison to the control device. While significant changes in OPV performance occur at low fluences, this is not reflected in the Raman spectra, the peak positions and intensity remain consistent, and there is no change in relative peak intensity or peak shape up to 10^{13} p cm^{-2} despite the PCE dropping to 0.7%. The intensity of the Raman spectra starts to increase slightly as the fluence is increased to 10^{14} p cm^{-2} and there is a further significant intensity increase at 10^{15} p cm^{-2} across the 1400–1600 cm^{-1} region. This indicates that the changes to the active layer components are very small under low fluence and that the full impact of proton irradiation on the photoactive layer occurs only after high irradiation fluence. However, we consider that the structural changes might have already happened at lower proton fluence, but not large enough to be probed by the Raman spectroscopy (supported by the photoelectrical measurements above at lower fluence).

The effect of proton irradiation on individual Raman peaks can be used to elucidate changes of individual molecular vibrations and point toward suggested pathways of structural change. There are small changes in the Raman signal of the PTB7-Th:$PC_{71}BM$ devices at 10^{14} p cm^{-2} and the same

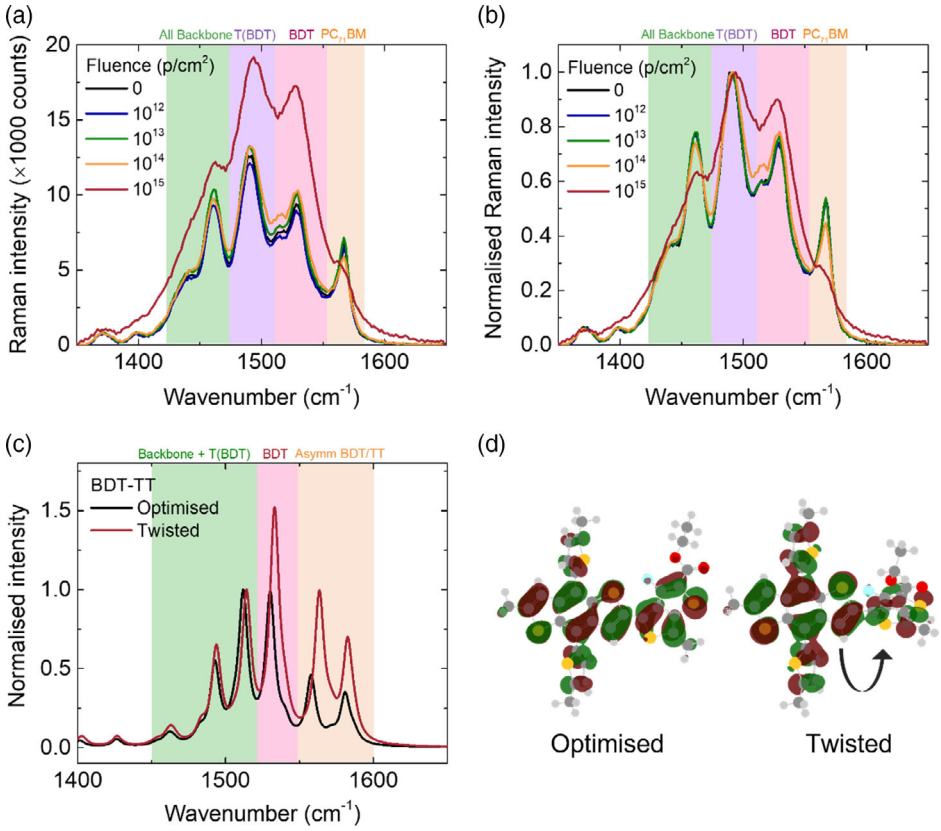

Figure 6. Raman spectroscopy at 532 nm excitation: a) Raman spectra of PTB7-Th:$PC_{71}BM$ devices; b) normalized Raman spectra, normalized to peak at 1491 cm^{-1}; c) simulations of the Raman spectra of PTB7-Th with optimized and twisted angle between the BDT and TT units, respectively; d) simulation of PTB7-Th HOMO with optimized and twisted angle between the BDT and TT units, showing loss of delocalization along the backbone.

signatures are further enhanced when irradiated with 10^{15} p cm^{-2} fluence. The intensity of the PTB7-Th BDT peaks increases and there is a peak broadening to higher wavenumber (Figure 6b) while the delocalized backbone peak increases slightly. In the normalized spectra, there is a blueshift of the T(BDT) peak to 1494 cm^{-1} and an increase in the relative peak intensity of the localized asymmetric BDT peak (1528 cm^{-1}), 0.9 with respect to the T(BDT) peak, while the peak (1461 cm^{-1}) originating from the delocalized backbone drops in intensity to 0.6. The enhancement of the asymmetric vibration of the BDT unit suggests that a degradation route might affect the symmetry of this unit. The strong reduction in intensity of the $PC_{71}BM$ peak at 1567 cm^{-1} may suggest the disruption of the C5/C6 rings within the fullerene cage after proton irradiation.[26]

The conformational change of the PTB7-Th backbone is further supported by DFT simulation. Increasing the angle between the BDT and TT units results in the same Raman signature changes (Figure 6c) as seen in the experimental data (Figure 6b). Such conformational change indicates a reduced effective conjugation length of the polymer (Figure 6(d)), increasing the energetic disorder. This proposed conformational change is consistent with the change observed in the device absorbance at high proton fluence (Figure 4b), where the blueshift indicated a shortening of effective conjugation length.

2.7. Nature of Insoluble Degradation Product

Figure 7 shows the normalized Raman spectra of the undissolved materials remaining on the bombarded devices after dissolution in chlorobenzene. The strong and well-defined peaks attributed to PTB7-Th show that there is a significant proportion of insoluble polymer remaining after dissolution. The peak changes mirror the progression of Raman signature changes observed in the device at higher fluence before dissolution (Figure 6). However, these peak shifts start at a lower fluence, suggesting that the degradation process has indeed started at least at 10^{13} p cm^{-2} (Figure 7a). These changes continue to develop in intensity as the fluence is increased to 10^{14} p cm^{-2} (Figure 7b) and at a fluence of 10^{15} p cm^{-2} (Figure 7c). At high fluence there is no change to the Raman peaks before and after redissolving, suggesting that the sample has become mostly cross-linked during high proton irradiation and is minimally affected by the washing. The absorbance of the solute at 10^{15} p cm^{-2} shows that only a very small fraction of both PTB7-Th and $PC_{71}BM$ are dissolved in chlorobenzene (Figure 5h). Therefore, it is expected that most of the active layer of the 10^{15} p cm^{-2} device should be insoluble and hence there is very little changes in the Raman spectrum after dissolution.

Higher performing OPV systems are practically more relevant to real applications of OPV cells in space. Before choosing

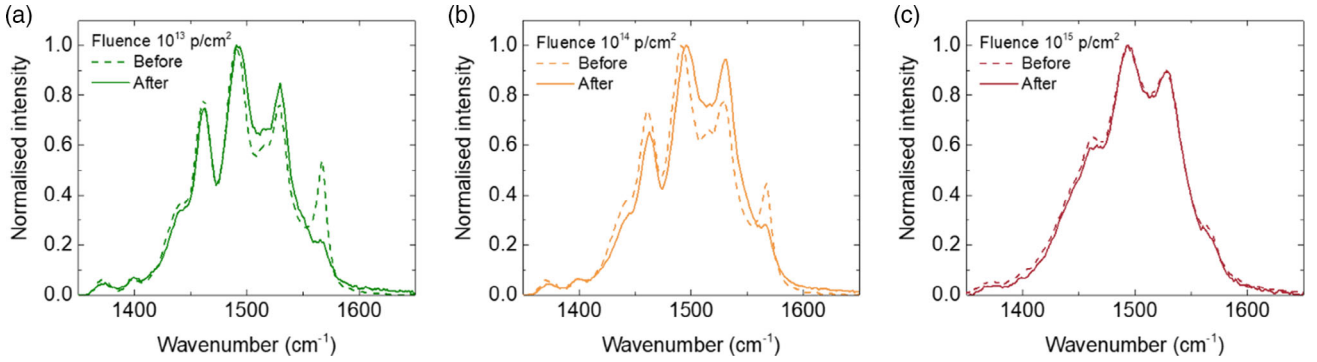

Figure 7. Normalized Raman spectra of devices that underwent fluence of a) 10^{13} p cm^{-2}, b) 10^{14} p cm^{-2}, and c) 10^{15} p cm^{-2} before and after redissolving.

PTB7-Th:$PC_{71}BM$ as the target system for this study, we in fact checked four more OPV systems, including some higher performance nonfullerene acceptor (NFA)-based systems in the system screening process. Those devices are examined with proton irradiation up to fluence of 10^{13} p cm^{-2}. Regrettably, for those systems incorporating NFA, there are considerable drops in PCE for the control devices which makes isolation of the degradation due to proton irradiation not possible. As a result, we did not select the state-of-the-art NFA systems for detail study despite desirable initial performance. The normalized PCE of all five OPV systems tested are shown in Figure S8, Supporting Information, for comparison. Overall, their degradation trends are similar, suggesting that the results obtained from PTB7-Th:$PC_{71}BM$ are highly relevant and representable.

2.8. Proton Radiation Hardness of OPV in Comparison with Inorganic PV

Ionizing radiation is not only harmful to OPV, but also inorganic PV. Silicon and GaAs PV are in fact not stable upon proton irradiation. Studies revealed that the performance of GaAs PV cells remained approximately 20–40% of the original performance after exposure to very similar conditions to our lowest fluence (10^{12} p cm^{-2} with proton energy of 100–200 keV).[33] For the five OPV systems tested in this work, the remaining PCE ranges from 48% to 76% (see Figure S8, Supporting Information), which are more radiation robust than the GaAs/III–V semiconductor PV cells which are currently the dominating PV technologies used for space missions. Despite the advantageous radiation resistance of the OPV materials, the primary stress factors such as oxygen and moisture are still relevant as they could affect the terrestrial shelf life.

3. Conclusion

In this study, we have chosen a wide range of fluence, from a low fluence of 10^{12} p cm^{-2} to a high fluence of 10^{15} p cm^{-2}. It is found that the device performance drops considerably at 10^{12} p cm^{-2} and 10^{13} p cm^{-2}, even worse at 10^{14} p cm^{-2} and 10^{15} p cm^{-2}. Optoelectrical characterizations (TPV and TPC) are able to probe the changes of the devices with low fluences and show that shallow traps are likely to be formed, resulting in higher charge recombination. However, for higher fluences, 10^{14} or 10^{15} p cm^{-2}, the optoelectrical properties of the devices seem to be ruined and result in poor extraction from the data. On the other hand, for spectroscopic characterizations, changes are mainly observed at higher fluences. Also, the degree of insolubility which can be linked to degradation of the active materials increases with increasing fluence.

To conclude, the radiation resistance of a benchmark OPV system, PTB7-Th:$PC_{71}BM$, against proton of 150 keV with fluence from 10^{12} to 10^{15} p cm^{-2} is examined. Although quite severe degradation was observed already after exposure to 10^{12} p cm^{-2}, the PCE remains 46% which show a higher remaining factor than GaAs cells. TPC and TPV results showed that shallow traps are likely to form at 10^{12} and 10^{13} p cm^{-2} while spectroscopic changes are not clear. For Raman spectroscopy, changes begin to be observed from 10^{14} p cm^{-2}. By redissolving the proton irradiated devices, the active layers are found to be not completely soluble from 10^{13} p cm^{-2}. This result is consistent with cross-linking which becomes more severe at higher fluences. Raman spectroscopy reveals conformational changes on the polymer PTB7-Th, showing a twisting between the BDT and the TT units after proton irradiation, which should lead to an increase in energetic disorder. This work not only provides an in-depth study on a benchmark OPV system PTB7-Th:$PC_{71}BM$ upon proton irradiation but also highlights the potential of using OPV cells for space mission in the future.

4. Experimental Section

Materials: Quartz substrates were purchased from Kintec. AZO target was purchased from Plasmaterials. PTB7-Th was purchased from 1-Material. $PC_{71}BM$ was purchased from Solenne BV. Chlorobenzene (CB), zinc acetate dihydrate, 2-methoxyethanol, and ethanolamine were purchased from Sigma-Aldrich. All materials were used as received.

Proton Simulation: The proton energy loss and the distribution of protons were performed by the Stopping and Range of Ions in Matter (SRIM).[34] The distribution of the stopping positions of 150 keV proton in the device configuration as shown in Figure 1b is simulated based on 10 000 protons.

Device Fabrication: Quartz substrates (Kintec, Hong Kong) were cleaned in an ultrasonic bath with Hellmanex (Sigma-Aldrich), deionized water, acetone, and then 2-propanol. AZO (≈700 nm) was RF-sputtered onto the cleaned quartz substrates using a Moorfield Nanolab 60 sputtering system with a power density of 2.46 W cm^{-2}. The sheet resistance of the AZO was 23–25 Ω sq^{-1}. ZnO layers were prepared by sol–gel method

and the precursor solution was spin-coated onto oxygen plasma-treated substrates. Detail of the preparation of the ZnO layer was reported previously.[35] The ZnO-coated substrates were then transferred into a nitrogen-filled glove box. PTB7-Th and $PC_{71}BM$ (1:1.5 by weight) were dissolved in chlorobenzene with 3 vol% of 1,8-diiodooctane at 60 °C with a total concentration of 25 mg mL^{-1} for at least 12 h. The PTB7-Th:$PC_{71}BM$ solution was spin-coated onto the ZnO layer at 1200 rpm for 60 s, resulting in a thickness of approximately 100 nm. The films were then transferred to an evaporator for MoO_3 (10 nm) and Ag (130 nm) evaporations. The resulting device area is 0.15 cm^2.

Proton Irradiation: Proton irradiations were performed at the Surrey Ion Beam Centre in the UK. The samples were sealed in a nitrogen-filled glove box and kept in the dark during transport. They were unpacked and expose to ambient air right before loading them into a vacuum chamber. The OPV cells were mounted directly onto 4 in. support plates that were inserted into a carousel wheel in the sample chamber. Silver paste was applied to allow charges to be conducted to the back of the samples and in the holder plate to avoid charge accumulation. Samples were loaded in a 7°/0° tilt/twist orientation to the incident beam and implanted under vacuum ($2.3 \pm 0.2 \times 10^{-6}$ mbar). The samples were placed to receive direct impact of the protons, with the back contact (silver electrode) facing the proton source. A Danfysik 1090 low-energy high-current implanter was used to implant 150 keV protons into the samples (from the silver side). The fluence rate was controlled to 3×10^{10} p cm^{-2}s for fluence 10^{12} and 3×10^{11} p cm^{-2}s for fluences 10^{13}–10^{15} p cm^{-2}. After the proton irradiation, the samples were packed and sent back for further characterizations.

Device Characterization: The unencapsulated devices were characterized in ambient air with temperature of 20−22 °C and relative humidity of 55–65%. *J–V* responses were measured using a sourcemeter (Keithley 2400) under a solar simulator (Newport 92193A-1000) with an AM0 or AM1.5G filter. EQE spectra were obtained using AC mode with a chopping frequency of 77 Hz by a quantum efficiency measurement system (PV Measurements QEX10). The EQE system was calibrated using a NIST traceable calibration cell (PV measurements). The reflection spectra were measured using a Perkin Elmer Lambda 750 spectrophotometer with an integrating sphere.

TPV/TPC Measurements: The devices were probed under white LED arrays to achieve 1 sun equivalent performance (calibrated using the J_{SC} values obtained from the 1 sun measurements). TPV measurements were performed using a commercially available transient measurement system (Automatic Research GmbH). This system uses a 520 nm green laser diode driven by a waveform generator (Keysight 33500B) to give a 300 ns pulse length. Background illumination was provided by a white LED with its intensity calibrated to generate the same device photocurrent as measured using the solar simulator—this intensity is referred to as "1 sun equivalent." An intensity range was then calibrated using a silicon photodiode. Transient responses were captured by a digital storage oscilloscope (Keysight DSOX2024A), the number of sample averages being adjusted to optimize signal noise and measurement time. The device under test was held at open circuit by a custom-built voltage follower (1.5 TΩ input impedance). TPC measurements were performed by using a high-speed transimpedance amplifier (Femto DHPCA-100). The charge carrier lifetime was calculated using a monoexponential fit to the TPV decay. The charge carrier density was calculated by integrating the capacitance with respect to voltage, with the capacitance calculated using the differential charging method, $C_{DC} = \Delta Q/\Delta V$, where ΔQ is obtained from the integral of the TPC decay and $\cdot V$ is the amplitude of the TPV transient, for the same laser pulse intensity.

AFM: AFM measurements were performed in tapping mode using a Veeco Dimension 3100 scanning force microscope equipped with a nanoscope 3 A feedback controller. TESPA-V2 (Bruker) cantilevers were used with a resonance of 320 kHz and spring constant of 42 N m^{-1}. All data were processed using Gwyddion software and roughness values were extracted using the Gwyddion statistical quantities tool.

Raman Characterization: Raman and photoluminescent measurements were performed using a Renishaw inVia Raman system (Renishaw plc., Wotton-Under-Edge, UK) in backscattering configuration. A 532 nm laser and a 50× objective were used (NA 0.50, spot size ≈1 μm). For Raman measurements, a laser power of 150 μW and an acquisition time of 10 s were used. For PL measurements, a laser power of 15 μW and an acquisition time of 10 s were used.

Raman Simulation: Raman peak assignment and degradation routes were simulated using DFT on the Imperial College High-Performance Computing service using GAUSSAIN09 software.[36] All simulations were performed on single molecules in the gas phase using B3LYP level of theory and basis set 6–31G(d,p).[37–40] Frequency of vibrations was identified from simulations of Raman spectra using empirical scaling factor of 0.97,[41] and peak assignments were visualized using GaussView 6.0.16 software.

Supporting Information

Supporting Information is available from the Wiley Online Library or from the author.

Acknowledgements

H.K.H.L. and K.S. contributed equally to this work. H.K.H.L., D.H., and W.C.T. would like to thank Airbus Endeavr Wales for their financial support. H.K.H.L., Z.W., T.M.W., and W.C.T. would like to acknowledge the support given to the SPECIFIC Innovation and Knowledge Centre by the Engineering and Physical Science Research Council (EP/N020863/1); Innovate UK (920036) and by the European Regional Development Fund (c80892) through the Welsh Government. K.S. and J.-S.K. would like to acknowledge the UK EPSRC for a studentship under DTG and the Centre for Doctoral Training in Plastic Electronic Materials (EP/L016702/1), and the Imperial College High Performance Computing Service for DFT calculations. This research was also supported by the UK EPSRC ATIP Programme Grant (EP/T028513/1) and the Global Research Laboratory Program of the National Research Foundation (NRF) funded by the Ministry of Science, ICT & Future Planning (NRF-2017K1A1A2 013153). A.P. and M.J.C. thank the Welsh European Funding Office (SPARC II) for funding.

Conflict of Interest

The authors declare no conflict of interest.

Data Availability Statement

The data that support the findings of this study are available from the corresponding author upon reasonable request.

Keywords

organic photovoltaics, proton bombardment, space

Received: December 7, 2021
Revised: January 25, 2022
Published online:

[1] Q. Liu, Y. Jiang, K. Jin, J. Qin, J. Xu, W. Li, J. Xiong, J. Liu, Z. Xiao, K. Sun, S. Yang, *Sci. Bull.* **2020**, *65*, 272.
[2] *Best Research-Cell Efficiency Chart. NREL* https://www.nrel.gov/pv/cell-efficiency.html (accessed: November 2021).
[3] M. Kaltenbrunner, M. S. White, E. D. Głowacki, T. Sekitani, T. Someya, N. S. Sariciftci, S. Bauer, *Nat. Commun.* **2012**, *3*, 770.

[4] H. Jinno, K. Fukuda, X. Xu, S. Park, Y. Suzuki, M. Koizumi, T. Yokota, I. Osaka, K. Takimiya, T. Someya, *Nat. Energy* **2017**, *2*, 780.
[5] S. Park, S. W. Heo, W. Lee, D. Inoue, Z. Jiang, K. Yu, H. Jinno, D. Hashizume, M. Sekino, T. Yokota, K. Fukuda, K. Tajima, T. Someya, *Nature* **2018**, *561*, 516.
[6] E. M. Speller, A. J. Clarke, J. Luke, H. K. H. Lee, J. R. Durrant, N. Li, T. Wang, H. C. Wong, J.-S. Kim, W. C. Tsoi, Z. Li, *J. Mater. Chem. A* **2019**, *7*, 23361.
[7] E. M. Speller, A. J. Clarke, N. Aristidou, M. F. Wyatt, L. Francàs, G. Fish, H. Cha, H. K. H. Lee, J. Luke, A. Wadsworth, A. D. Evans, I. McCulloch, J.-S. Kim, S. A. Haque, J. R. Durrant, S. D. Dimitrov, W. C. Tsoi, Z. Li, *ACS Energy Lett.* **2019**, *4*, 846.
[8] H. K. H. Lee, A. M. Telford, J. A. Röhr, M. F. Wyatt, B. Rice, J. Wu, A. de Castro Maciel, S. M. Tuladhar, E. Speller, J. McGettrick, J. R. Searle, S. Pont, T. Watson, T. Kirchartz, J. R. Durrant, W. C. Tsoi, J. Nelson, Z. Li, *Energy Environ. Sci.* **2018**, *11*, 417.
[9] G. Li, Y. Yang, R. A. B. Devine, C. Mayberry, *Nanotechnology* **2008**, *19*, 424014.
[10] A. Kumar, R. Devine, C. Mayberry, B. Lei, G. Li, Y. Yang, *Adv. Funct. Mater.* **2010**, *20*, 2729.
[11] A. Kumar, N. Rosen, R. Devine, Y. Yang, *Energy Environ. Sci.* **2011**, *4*, 4917.
[12] K. Kambour, N. Rosen, C. Kouhestani, M. C Duc Nguyen, R. A. B. Devine, A. Kumar, C.-C. Chen, G. Li, Y. Yang, *IEEE Trans. Nucl. Sci.* **2012**, *59*, 2902.
[13] A. K. Thomas, C. J. Kouhestani, J. K. Grey, *Sol. Energy Mater. Sol. Cells* **2017**, *160*, 85.
[14] I. V. Martynov, A. V. Akkuratov, S. Y. Luchkin, S. A. Tsarev, S. D. Babenko, V. G. Petrov, K. J. Stevenson, P. A. Troshin, *ACS Appl. Mater. Interfaces* **2019**, *11*, 21741.
[15] F. Bebensee, J. Zhu, J. H. Baricuatro, J. A. Farmer, Y. Bai, H.-P. Steinrück, C. T. Campbell, J. M. Gottfried, *Langmuir* **2010**, *26*, 9632.
[16] H. O. Lee, M. Hasib, S. S. Sun, *Radiat. Eff. Defects Solids* **2017**, *172*, 355.
[17] J. Barbé, H. K. H. Lee, H. Toyota, K. Hirose, S.-I. Sato, T. Ohshima, K. C. Heasman, W. C. Tsoi, *Appl. Phys. Lett.* **2018**, *113*, 183301.
[18] I. Cardinaletti, T. Vangerven, S. Nagels, R. Cornelissen, D. Schreurs, J. Hruby, J. Vodnik, D. Devisscher, J. Kesters, J. D'Haen, A. Franquet, V. Spampinato, T. Conard, W. Maes, W. Deferme, J. V. Manca, *Sol. Energy Mater. Sol. Cells* **2018**, *182*, 121.
[19] L. K. Reb, M. Böhmer, B. Predeschly, S. Grott, C. L. Weindl, G. I. Ivandekic, R. Guo, C. Dreißigacker, R. Gernhäuser, A. Meyer, P. Müller-Buschbaum, *Joule* **2020**, *4*, 1880.
[20] M. F. Bartusiak, J. Becher, *Appl. Opt.* **1979**, *18*, 3342.
[21] P. Jiggens, D. Heynderickx, I. Sandberg, P. Truscott, O. Raukunen, R. Vainio, *J. Space Weather Space Clim.* **2018**, *8*, 22.
[22] A. Pockett, H. K. H. Lee, M. J. Carnie, B. L. Coles, W. C. Tsoi, *Nanoscale* **2019**, *11*, 10872.
[23] H. K. H. Lee, J. Wu, J. Barbé, S. M. Jain, S. Wood, E. M. Speller, Z. Li, F. A. Castro, J. R. Durrant, W. C. Tsoi, *J. Mater. Chem. A* **2018**, *6*, 5618.
[24] A. J. Mozer, N. S. Sariciftci, L. Lutsen, D. Vanderzande, R. Österbacka, M. Westerling, G. Juška, *Appl. Phys. Lett.* **2005**, *86*, 112104.
[25] J. Wu, J. Luke, H. K. H. Lee, P. Shakya Tuladhar, H. Cha, S.-Y. Jang, W. C. Tsoi, M. Heeney, H. Kang, K. Lee, T. Kirchartz, J.-S. Kim, J. R. Durrant, *Nat. Commun.* **2019**, *10*, 5159.
[26] J. Wu, H. Cha, T. Du, Y. Dong, W. Xu, C-Ting Lin, J. R. Durrant, *Adv. Mater.* **2021**, *34*, 2101833.
[27] C. H. Peters, I. T. Sachs-Quintana, W. R. Mateker, T. Heumueller, J. Rivnay, R. Noriega, Z. M. Beiley, E. T. Hoke, A. Salleo, M. D. McGehee, *Adv. Mater.* **2012**, *24*, 663.
[28] H. Cha, J. Wu, A. Wadsworth, J. Nagitta, S. Limbu, S. Pont, Z. Li, J. Searle, M. F. Wyatt, D. Baran, J.-S. Kim, I. McCulloch, J. R. Durrant, *Adv. Mater.* **2017**, *29*, 1701156.
[29] S. R. Cowan, A. Roy, A. J. Heeger, *Phys. Rev. B* **2010**, *82*, 245207.
[30] A. Armin, G. Juska, M. Ullah, M. Velusamy, P. L. Burn, P. Meredith, A. Pivrikas, *Adv. Mater.* **2014**, *4*, 1300954.
[31] D. R. Coulter, A. Gupta, M. V. Smith, R. E. Fornes, *Effects of energetic proton bombardment on polymeric materials: Experimental studies and degradation models*, National Aeronautics and Space Administration, Jet Propulsion Laboratory Publication, California Institute of Technology, Pasadena, California **1986**.
[32] O. R. Yamilova, I. V. Martynov, A. S. Brandvold, I. V. Klimovich, A. H. Balzer, A. V. Akkuratov, I. E. Kusnetsov, N. Stingelin, P. A. Troshin, *Adv. Mater.* **2020**, *10*, 1903163.
[33] B. E. Anspaugh, in *The Conf. Record of the Twenty-Second IEEE Photovoltaic Specialists Conf. – 1991*, IEEE, Las Vegas, NV, USA, **1991**, pp. 1593–1598, https://doi.org/10.1109/PVSC.1991.169472.
[34] J. F. Ziegler, SRIM, http://www.srim.org/ (accessed: June 2020).
[35] A. Way, J. Luke, A. D. Evans, Z. Li, J.-S. Kim, J. R. Durrant, H. K. Hin Lee, W. C. Tsoi, *AIP Adv.* **2019**, *9*, 085220.
[36] M. J. Frisch, et al. GAUSSIAN09, Revision A.1., **2009**.
[37] A. D. Becke, *J. Chem. Phys.* **1993**, *98*, 5648.
[38] G. A. Petersson, M. A. Al-Laham, *J. Chem. Phys.* **1991**, *94*, 6081.
[39] G. A. Petersson, A. Bennett, T. G. Tensfeldt, M. A. Al-Laham, W. A. Shirley, J. A. Mantzaris, *J. Chem. Phys.* **1988**, *89*, 2193.
[40] P. J. Stephens, F. J. Devlin, C. F. Chabalowski, M. J. Frisch, *J. Phys. Chem.* **1994**, *98*, 11623.
[41] M. L. Laury, M. J. Carlson, A. K. Wilson, *J. Comput. Chem.* **2012**, *33*, 2380.